

Simulation of high Rayleigh number natural convection in a square cavity using the lattice Boltzmann method

H.N. Dixit, V. Babu *

Thermodynamics and Combustion Engineering Laboratory, Department of Mechanical Engineering, Indian Institute of Technology Madras, Chennai 600 036, India

Received 4 February 2005; received in revised form 14 July 2005
Available online 20 October 2005

Abstract

A thermal lattice Boltzmann method based on the BGK model has been used to simulate high Rayleigh number natural convection in a square cavity. The model uses the double populations approach to simulate hydrodynamic and thermal fields. The traditional lattice Boltzmann method on a uniform grid has unreasonably high grid requirements at higher Rayleigh numbers which renders the method impractical. In this work, the interpolation supplemented lattice Boltzmann method has been utilized. This is shown to be effective even at high Rayleigh numbers. Numerical results are presented for natural convection in a square cavity with insulated horizontal walls and isothermal vertical walls maintained at different temperatures. Very fine grids (wall $y^+ < 0.3$) have been used for the higher Rayleigh number simulations. A universal structure is shown to exist in the mean velocity turbulent boundary layer profile for $y^+ < 10$. This agrees extremely well with previously reported experimental data. The numerical results (for Rayleigh numbers up to 10^{10}) are in very good agreement with the benchmark results available in the literature. The highlight of the calculations is that no turbulence model has been employed.

© 2005 Elsevier Ltd. All rights reserved.

1. Introduction

In the last decade and a half, tremendous amount of research has been carried out in discrete lattice kinetic theory, and in particular, the lattice Boltzmann method (LBM). Lattice Boltzmann method has become a novel alternative to traditional numerical methods like finite difference, finite element and finite volume methods for solving the Navier–Stokes equations [1]. LB method has already found extensive applications in simulating physical phenomena of various complexities [2]. Of particular relevance to the present work is the simulation of temperature fields in both square [3,4] and tall cavities [5]. Lattice Boltzmann simulations have met with significant amount of success in the case of isothermal flows, and recently there have been a few attempts to show the feasibility of non-isothermal flow simulations using LBM. Some of the earliest works in thermal

lattice Boltzmann method include those of Alexander et al. [6], Chen et al. [7] and Eggels and Somers [8]. Thermal lattice Boltzmann models can be classified into three categories based on their approach in solving the Boltzmann equation, namely, the multispeed, the passive scalar and the thermal energy distribution approach.

The multispeed approach, is an extension of the common LBE isothermal models in which only the density distribution function is used. To obtain the temperature evolution equation at the macroscopic level, additional speeds are necessary and the equilibrium distribution must include the higher-order velocity terms, i.e., it is theoretically possible to express both heat flux and temperature in terms of higher-order kinetic moments of the particle distribution functions $f(\vec{x}, t)$. Higher-order velocity terms are involved in the formulation of the polynomial equilibrium distribution and additional speeds are required on the corresponding lattices. But, the inclusion of higher order velocity terms leads to numerical instabilities and hence the temperature variation is limited to a narrow range [9].

* Corresponding author. Tel.: +91 44 22574688.
E-mail address: vbabu@iitm.ac.in (V. Babu).

Nomenclature

f, g	single particle distribution function for density and internal energy	Pr	$\frac{\nu}{\chi}$, Prandtl number
f^{eq}, g^{eq}	equilibrium distribution function for density and internal energy	Ra	$\frac{\beta g \Delta T H^3}{\nu \chi}$, Rayleigh number
w_i	weights for the particle equilibrium distribution function	<i>Greek symbols</i>	
\vec{u}	macroscopic velocity	β	coefficient of thermal expansion
\vec{u}	slip velocity at the boundary	ν	kinematic viscosity
(U_w, V_w)	wall velocity	χ	thermal diffusivity
c	dx/dt , the minimum speed on the lattice	ρ	fluid density
T, T_m	local and average temperatures	$\hat{\rho}$	density corresponding to the slip velocity
T_h, T_c	hot and cold wall temperatures	τ_v, τ_c	single particle relaxation times for density and internal energy
H	height and width of the cavity	$\vec{\zeta}$	particle velocity
k	thermal conductivity	<i>Subscripts and superscripts</i>	
g	acceleration due to gravity	w	wall
F	external force (buoyancy force)	i	lattice link number
Ma	Mach number	eq	equilibrium
Nu_0	$-\frac{H}{\Delta T} \frac{\partial T}{\partial x}$, Nusselt number		

The passive-scalar approach utilizes the fact that the macroscopic temperature satisfies the same evolution equation as a passive scalar if the viscous heat dissipation and compression work done by the pressure are negligible [10,11]. In this scheme, temperature is simulated using a separate distribution function which is independent of the density distribution. This approach has attracted much attention compared to the multispeed approach on account of its numerical stability. But the main disadvantage is that viscous heat dissipation and compression work done by pressure cannot be incorporated in this model.

The work of He and Luo [12] showed that the isothermal lattice Boltzmann equation can be directly obtained by properly discretizing the continuous Boltzmann equation in both time and phase space. The equilibrium distribution f^{eq} has a fixed form which depends on the discretized velocity set chosen. The f^{eq} is obtained by adjusting the coefficients in the polynomial so as to reproduce the Navier–Stokes equations, but stability is not considered. This type of construction works well for an isothermal model because the deviation of f^{eq} from the Maxwell–Boltzmann equilibrium is $O(u^2)$. In the case of a non-isothermal model, this deviation is only $O(u)$ which is clearly insufficient. Hence in constructing a LBE thermal model, the equilibrium distribution function f^{eq} should not only lead to the incompressible Navier–Stokes equation, but should also satisfy the Maxwell–Boltzmann equilibrium so that the stability of the model is assured by the H -theorem. This has led to the development of the thermal energy distribution model called the “doubled population model”. Here the thermal lattice Boltzmann evolution equation is derived by properly discretizing the continuous Boltzmann equation for the internal energy distribution [13].

It has been shown [13] that both the thermal energy and heat flux can be expressed as kinetic moments of a new thermal energy distribution function, $g(\vec{x}, t)$. The zeroth order moment of g gives the internal energy and the first order moment gives the heat flux. The advantage of employing such a method is that no moments higher than first order is ever required, thus providing numerical stability.

Extensive studies have been carried out on natural convection in enclosures—numerical studies of de Vahl Davis [14] for the laminar flow cases and numerical studies by Henkes and Hoogendoorn [15] and Marakatos and Pericleous [16] for transition and turbulent flow cases and pseudo spectral studies of Le Quéré [17]. The flow is laminar for Rayleigh numbers (Ra) less than 10^6 and it undergoes transition for $10^6 < Ra < 10^8$ and then the flow becomes fully turbulent.

A few researchers have carried out simulations of this flow using LBM. Peng et al. [3] simulated natural convection in square cavity using a simplified thermal model. In this model, the complex gradient operator present in the evolution equation of the temperature was eliminated. D’Orazio et al. [4] have also carried out LBM calculations for the same problem, but with a general purpose thermal boundary condition, to handle both Dirichlet and Neumann boundary conditions. Again, the Rayleigh numbers simulated were limited to the laminar case only.

To date, LBM simulations of fully turbulent natural convection at very high Rayleigh numbers have not been reported, presumably due to the enormous grid requirements. In the present study, simulations up to $Ra = 10^{10}$ have been carried out and validated with solutions available in the literature, thus establishing the robustness of the LBM calculations. It must be emphasized that no tur-

bulent model has been used in the present study. Though the problem of natural convection in a square cavity is not new in the LBM community, not much progress has been made in terms of the Rayleigh numbers simulated. All the previous researchers have used uniform grids in their simulations which restricts the Rayleigh numbers that can be simulated. Use of irregular lattices in LB calculations was shown first by Nannelli and Succi [18]. In the present work, the Interpolation Supplemented Lattice Boltzmann (ISLB) Method [19] which allows LBM simulations on non-uniform grids, has been used. The importance of using non-uniform grids in conjunction with LBM has been discussed by Eggels and Somers [8].

In the present work, the thermal lattice Boltzmann scheme proposed by He et al. [13] is used for simulating natural convection of a Boussinesq fluid in a square cavity. The main drawback in using this model is the doubling of the memory requirement for the simulations owing to the use of two separate distribution functions. To alleviate this, continuously varying non-uniform grids have been employed in the present work which results in considerable reduction in the grid requirement. Also a grid independence study has been carried out for the thermal ISLBM at a high Rayleigh number. The main objective of the present work is to establish lattice Boltzmann method as a viable tool for the simulation of temperature fields at very high Rayleigh numbers and demonstrate the usefulness of the fully non-uniform grids.

This paper is organized as follows. In Section 2, a brief overview of the thermal model employed along with a simple discussion of the boundary conditions used in the present simulations is given. Section 3 presents an overview and the computational details of the ISLB method. In Section 4, results are presented and discussed for both uniform as well as non-uniform grids. Section 5 concludes the paper.

2. Overview of thermal LBM

In the doubled population approach, the flow and the temperature fields are solved by two separate evolution equations, both of which, at the macroscopic level yield the Navier–Stokes equation and the energy equation through an appropriate Chapman–Enskog expansion. The main drawbacks with this approach is the use of the BGK (single-relaxation time) approximation, which restricts the Prandtl number to a very narrow range, and doubling of memory requirement.

Kinetic theory states that the evolution of the single-particle density distribution in a fluid system obeys the Boltzmann equation

$$\partial_t f + (\vec{\xi} \cdot \nabla) = \Omega(f) \tag{1}$$

where f is the single-particle density distribution function, $\vec{\xi}$ is the microscopic velocity, and Ω is the collision term. After including the effect of external forces and using the BGK approximation, the above equation becomes

$$\partial_t f + (\vec{\xi} \cdot \nabla) = -\frac{f - f^{eq}}{\tau_v} + F \tag{2}$$

Here τ_v is the relaxation time and f^{eq} is the Maxwell–Boltzmann equilibrium distribution given by

$$f^{eq} = \frac{\rho}{(2\pi RT)^{D/2}} \exp\left[-\frac{(\vec{\xi} - \vec{u})^2}{2RT}\right] \tag{3}$$

where R is the gas constant and D is the dimensionality of the solution space under consideration. Macroscopic variables, such as the density ρ , and velocity \vec{u} can be calculated as the moments of the density distribution function:

$$\rho(\vec{x}, t) = \int f(\vec{x}, \vec{\xi}, t) d\vec{\xi} \tag{4}$$

$$\rho(\vec{x}, t)\vec{u}(\vec{x}, t) = \int \vec{\xi} f(\vec{x}, \vec{\xi}, t) d\vec{\xi} \tag{5}$$

Similarly, the evolution equation for internal energy is given as follows:

$$\partial_t g + (\vec{\xi} \cdot \nabla) = -\frac{g - g^{eq}}{\tau_c} \tag{6}$$

where τ_c is the relaxation time for the internal energy distribution function and

$$g(\vec{x}, \vec{\xi}, t) = \frac{(\vec{\xi} - \vec{u})^2}{2} f \tag{7}$$

The internal energy \vec{e} can be calculated as a moment of the internal energy distribution function g as

$$\rho(\vec{x}, t)\vec{e}(\vec{x}, t) = \int g(\vec{x}, \vec{\xi}, t) d\vec{\xi} \tag{8}$$

The temperature and internal energy are related through the equation of state $e = RT$. In all the simulations, a 9-bit two dimensional (D2Q9) lattice has been employed (Fig. 1). After a suitable discretization is carried out, the governing equations for the simplified thermal energy distribution model become

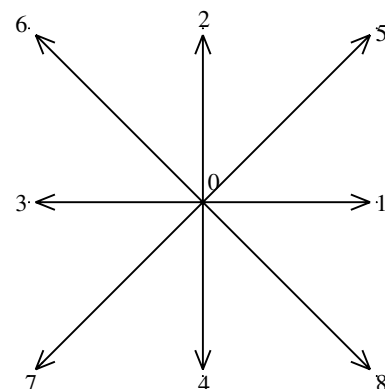


Fig. 1. D2Q9 Discrete velocity set.

$$f_i(\vec{x} + \vec{\xi}_i \delta t, t + \delta t) - f_i(\vec{x}, t) = -\frac{1}{\tau_v} [f_i(\vec{x}, t) - f_i^{\text{eq}}(\vec{x}, t)] + \delta t \cdot F_i \quad (9)$$

$$g_i(\vec{x} + \vec{\xi}_i \delta t, t + \delta t) - g_i(\vec{x}, t) = -\frac{1}{\tau_c} [g_i(\vec{x}, t) - g_i^{\text{eq}}(\vec{x}, t)] \quad (10)$$

Using the 9-bit two dimensional (D2Q9) lattice for which,

$$\vec{\xi}_i = \begin{cases} 0, & i = 0 \\ c\{\cos((i-1)\pi/2), \sin((i-1)\pi/2)\}, & i = 1, 2, 3, 4 \\ \sqrt{2}c\{\cos[(i-5)\pi/2 + \pi/4], \sin[(i-5)\pi/2 + \pi/4]\}, & i = 5, 6, 7, 8 \end{cases} \quad (11)$$

where $c = \sqrt{3RT}$ is the lattice speed. The equilibrium function for the density distribution function is given as

$$f_i^{\text{eq}} = w_i \rho \left[1 + \frac{3(\vec{\xi}_i \cdot \vec{u})}{c^2} + \frac{9(\vec{\xi}_i \cdot \vec{u})^2}{2c^4} - \frac{3\vec{u}^2}{2c^2} \right] \quad (12)$$

where $w_0 = 4/9$, $w_0 = 1/9$ for $i = 1, 2, 3, 4$ and $w_i = 1/36$ for $i = 5, 6, 7, 8$. Similarly, the equilibrium distribution for the new thermal energy distribution function g can be written as

$$g_0^{\text{eq}} = -\frac{2\rho e}{3} \frac{\vec{u}^2}{c^2} \quad (13)$$

$$g_{1,2,3,4}^{\text{eq}} = \frac{\rho e}{9} \left[\frac{3}{2} + \frac{3}{2} \frac{\vec{\xi}_i \cdot \vec{u}}{c^2} + \frac{9}{4} \frac{(\vec{\xi}_i \cdot \vec{u})^2}{c^4} - \frac{3}{2} \frac{\vec{u}^2}{c^2} \right] \quad (14)$$

$$g_{5,6,7,8}^{\text{eq}} = \frac{\rho e}{36} \left[3 + 6 \frac{\vec{\xi}_i \cdot \vec{u}}{c^2} + \frac{9}{2} \frac{(\vec{\xi}_i \cdot \vec{u})^2}{c^4} - \frac{3}{2} \frac{\vec{u}^2}{c^2} \right] \quad (15)$$

The macroscopic density, velocity and temperature are calculated from

$$\rho = \sum_i f_i \quad (16)$$

$$\rho \vec{u} = \sum_i \vec{\xi}_i f_i \quad (17)$$

$$\rho e = \sum_i g_i \quad (18)$$

A Chapman–Enskog expansion for the density distribution function recovers the Navier–Stokes equation from the evolution LBM equation. This gives the kinematic viscosity ν in terms of the single relaxation time for hydrodynamics τ_v as

$$\nu = \left(\tau_v - \frac{1}{2} \right) c^2 \delta t \quad (19)$$

A similar procedure for the thermal evolution equation of LBM yields the thermal diffusivity χ in terms of the single relaxation time for a non-isothermal flow, τ_c as

$$\chi = \frac{2}{3} \left(\tau_c - \frac{1}{2} \right) c^2 \delta t. \quad (20)$$

2.1. Non-dimensional parameters

In the simulation of natural convection, the external force term F corresponding to the buoyancy force is given by the expression $F = (\vec{G} \cdot (\vec{\xi} - \vec{u})/RT)f^{\text{eq}}$ with \vec{G} being the external force acting per unit mass [13]. In a natural convection problem, $\vec{G} = \rho\beta g(T - T_m)\vec{j}$, where \vec{j} is in a direction opposite to gravity.

With the Boussinesq approximation, all the fluid properties are constant except in the body force term where the fluid density varies as $\rho = \bar{\rho}[1 - \beta(T - T_m)]$ where $\bar{\rho}$ is the density of the fluid at the mean temperature T_m . In the case of natural convection, the flow and the temperature field depend on two non-dimensional parameters, namely, the Prandtl number and the Rayleigh number. For the LB simulation these two parameters are not enough to determine τ_v and τ_c because β is not known for a lattice fluid. However, in the case of LB simulations an additional dimensionless parameter, namely, Mach number is also relevant. For all the simulations presented here, the Mach number is set to be equal to 0.1 to make sure that the flow is fully in the incompressible regime. The Mach number is given as $Ma = |\vec{u}|/C_s$, where $|\vec{u}|$ and C_s are the characteristic velocity $\left(= [\beta g \Delta T H]^{\frac{1}{2}} \right)$ of the flow and the speed of sound respectively. This relation is used to find the value of β . All the velocities obtained in the simulation are normalized with the reference velocity χ/H , which is given as

$$\frac{\chi}{H} = \left[\frac{\beta g \Delta T H}{RaPr} \right]^{\frac{1}{2}} = \frac{Ma C_s}{(RaPr)^{\frac{1}{2}}} \quad (21)$$

The heat flux along the x -direction at any point in the domain is equal to $uT - \chi(\partial T/\partial x)$. Using the above definition, Nusselt number at various planes can be easily calculated by employing a numerical integration procedure.

2.2. Boundary conditions

No-slip boundary condition has been imposed on all the walls (Fig. 2). The horizontal walls are insulated and the vertical walls are maintained at constant, but different temperatures. In the present work, only Dirichlet type boundary conditions have been considered and the insulated boundary condition is simulated by converting it to Dirichlet type using a second order accurate finite-difference approximation. The boundary conditions have been implemented by using the counter-slip approach proposed by Inamuro et al. [20]. Although the suitability of the counter-slip approach has only been established for the hydrodynamic boundary conditions [21], in the present work, it has been utilized for modelling thermal boundary conditions as well. This requires very careful consideration as it has a tremendous effect on the predicted values of the wall Nusselt number. It was noted during the current simulations, that the traditional implementation of the Dirichlet boundary condition gave rise to a spurious gradient in

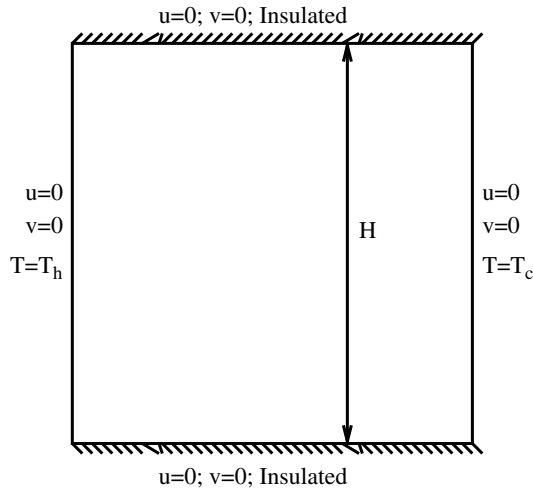


Fig. 2. Schematic illustration of square cavity with boundary conditions.

the temperature between the wall and the first point in the fluid. This gradient was a steep drop in the temperature near the hot wall and the cold wall and it persisted even after decreasing the mesh spacing by a factor of 8. This clearly implies that the source of this phenomenon is the implementation of the boundary condition and not the grid spacing. It follows that the simulations would then be effectively for a lower value of Rayleigh number than the one being prescribed. This, in turn, would yield incorrect values of wall Nusselt number. To overcome this difficulty, the counter-slip approach has been used for simulating the Dirichlet boundary condition also. The implementation details of the counter-slip approach are given in Ref. [22].

3. Implementation on non-uniform grids

In the traditional LB method, the particles reside on a uniform *lattice* with spacing determined by N_{char} where N_{char} is the number of grid points along the characteristic length (which is the height of the cavity, for the present case) if a uniform grid had been employed. As the Rayleigh number increases, the value of N_{char} increases, making the lattice spacing finer. At very high Rayleigh numbers, using a uniform grid increases the number of nodes considerably. This results in an increase in the operation count as well as memory requirement. To alleviate this difficulty, a *computational grid* which is different from the lattice is utilized in the Interpolation Supplemented Lattice Boltzmann method of He et al. [19]. The particle distribution functions are evaluated and stored only on the nodes of the *computational grid*. This grid can be non-uniform and so allows the computational nodes to differ from the uniform lattice. Thus the increase in the number of nodes with increasing Rayleigh number is not quite as high as before. However, as the particles undergo collision and advection on the lattice, determination of the distribution functions on the *computational grid* requires an interpolation procedure. The particle distribution function at each node of the *computational grid* can be determined by using second order

accurate upwind (based on the direction of the particle velocity, not the fluid velocity) interpolation.

In the present study, ISLBM is employed for all the high Rayleigh number cases, $Ra \geq 10^6$. The non-uniform grid used in the study follows a geometric progression for the grid spacing. The finest grid spacing is provided near the wall so as to properly resolve the boundary layers. It is important to use a smoothly varying grid with the finest grid spacing decided based on stability requirements. During each time step, the particles on the lattice undergo collision followed by advection as dictated by the lattice-BGK model. The particle distribution function at each node of the computational grid can then be determined by using second order accurate Lagrangian interpolation. This operation is carried out for both the density as well as internal energy distribution functions. The particle distributions on the boundary nodes of the computational grid are modified next according to the imposed boundary conditions. The operation count of the thermal ISLBM approach used here comes out to be about 500 floating point operations per node per time step. Of these, 200 operations arise from the interpolation operation. Thus, the use of a non-uniform grid, results in an increase of 66% in the number of floating point operations. However, the savings in the number of nodes more than offsets this increase, as will be shown in the next section.

4. Results and discussion

This section is divided into two parts. The first part deals with laminar natural convection studies on a uniform grid. The next part deals with higher Rayleigh number simulations using the ISLB scheme. The two main attractive features of the present implementation are (a) the absence of any turbulence model and, (b) the ability to use non-uniform grids.

Grid independence of the results has been established for two different Rayleigh numbers, namely, 10^4 and 10^8 . The variation of the magnitude and the location of the maximum x -velocity along the vertical centerline, the y -velocity along the horizontal centerline and the average Nusselt number with changing grid size are shown in Tables 1 and 2.

Table 1 gives the results obtained for the simulation of $Ra = 10^4$ on three grids and these have been compared with the benchmark results of de Vahl Davis [14] and Table 2

Table 1
Grid-dependence study for natural convection in square cavity at $Ra = 10^4$

Mesh	(64 × 64)	(128 × 128)	(256 × 256)	de Vahl Davis [14]
U_{max}	16.164	16.172	16.179	16.178
Y	0.828	0.820	0.824	0.823
V_{max}	19.569	19.599	19.619	19.617
X	0.125	0.117	0.121	0.178
\bar{Nu}	2.256	2.249	2.245	2.243

Table 2
Grid-dependence study for natural convection in square cavity at $Ra = 10^8$

Mesh	(256 × 256)	(512 × 512)	Henkes and Hoogendoorn [15]	Le Quéré [17]
U_{\max}	389.877	373.843	304.059	321.9
Y	0.937	0.933	–	0.928
V_{\max}	2241.37	2256.48	2229.55	2221.9
X	0.0112	0.0112	–	0.012
\overline{Nu}	29.540	30.156	30.20	30.225

compares the results obtained for $Ra = 10^8$ on two different grids with the work of Henkes and Hoogendoorn [15] and Le Quéré [17]. The maximum change in these metrics as a result of using the finer mesh is only 0.5% for $Ra = 10^4$ and about 2% for $Ra = 10^8$. Hence the results can be taken to be grid independent.

4.1. Salient features of the flow field

The problem of natural convection in a square cavity has been studied extensively and detailed explanations for various flow structures can be found in the literature. A unified description of the flow field from the laminar through the transitional to the turbulent regime is provided here. The flow is characterised by fluid moving up the hot wall and down the cold wall with a central region called the ‘core’ which becomes distinguishable at higher Rayleigh numbers.

At low Rayleigh numbers ($Ra \sim 10^3$), the flow is predominantly conduction dominated. This can be inferred from the relative magnitude of the diffusion term in the Navier–Stokes equation in comparison to the convection term which scales as $1/Ra$. As the Rayleigh number is increased, the relative magnitude of the convective term increases resulting in a shift from the conduction type flow. At these Rayleigh numbers ($Ra \geq 10^5$), the flow is characterised by distinct boundary layers along the hot and cold walls. The flow in the core region becomes parallel as depicted by the streamlines which are horizontal. As the Rayleigh number is further increased ($Ra \geq 10^7$), the bulk of the fluid motion takes place in the thin boundary layer along the hot and cold walls. Thinning of boundary layer occurs with an increase in Rayleigh number resulting in steeper velocity and temperature gradients. The temperature in the core region becomes increasingly stratified with very little vertical velocity in this region compared to the velocity in the boundary layers as depicted by horizontal streamlines in the core. Also, the maximum velocity position moves closer to the wall.

The upper-left and bottom-right corners form a barrier to the fast moving fluid resulting in flow separation downstream of the flow. At very high Rayleigh numbers, flow reversal occurs resulting in the formation of strong vortices at these corners. The core region and the adiabatic walls are connected through the horizontal boundary layers. The horizontal boundary layers along the adiabatic walls

are distinct from vertical boundary layers and boundary layer approximations cannot be used in this region. More detailed discussion on the flow field and the associated scaling can be found in Henkes and Hoogendoorn [15].

4.2. $10^3 \leq Ra \leq 10^6$

Table 3 compares the predictions from the present calculation with the literature results. The maximum horizontal velocity on the vertical midplane of the cavity, U_{\max} , and the corresponding y -coordinate, the maximum vertical velocity on the horizontal midplane of the cavity, V_{\max} , and the corresponding x -coordinate, and the average Nusselt number throughout the cavity \overline{Nu} , Nusselt numbers at the mid-plane and the left wall are compared for Rayleigh numbers less than 10^6 . The grid used for these simulations is also given in the table. All these results are in excellent agreement with the benchmark results of de Vahl Davis [14]. Figs. 3 and 4 show the isotherms and streamlines for $Ra = 10^3, 10^4, 10^5$ and 10^6 . The thermal and the flow fields also agree very well with those reported in the literature.

Fig. 5 shows the variation of non-dimensional temperature, $\left(= \frac{T-T_c}{T_h-T_c} \right)$ along the horizontal centerline of the cavity for the laminar flow simulations. It can be clearly seen that the steep variation of the temperature near the walls is resolved quite well.

4.3. $10^7 \leq Ra \leq 10^{10}$

As mentioned in Table 3, a 512×512 grid has been employed in the present work for simulating $Ra = 10^6$. Though this grid size bigger than usual for this Rayleigh number, the same Rayleigh number can be simulated on a grid as small as 128×128 when using ISLBM, as shown in Table 4. It is possible to use higher order interpolation schemes to obtain more accuracy, but the results shown here demonstrate that a second order interpolation is sufficient for these kinds of simulations.

Table 4 compares the results from the present calculations with those available in the literature for Rayleigh numbers up to 10^{10} . The agreement is within 5% for each metric considered, demonstrating the accuracy of the present calculations. A non-uniform grid with very fine mesh spacing at the walls have been used for the present simulations which results in very low values for the wall y^+ . These low values for y^+ (< 0.3) imply that the present calculations are able to resolve even the laminar sub-layer. More details regarding the wall resolution will be discussed in Section 4.4.

Values of N_{char} for each case are also given in Table 4. From the definition of N_{char} given earlier, it is easy to see that if a uniform grid had been employed for these calculations, the grid size would have been $N_{\text{char}} \times N_{\text{char}}$. For the values of N_{char} indicated in Table 4, and based on the operation count given in the previous section, it is evident that the uniform grid calculations will be prohibitively expensive for these Rayleigh numbers.

Table 3
Comparison of the numerical results of the present study with the benchmark solution of de Vahl Davis [14]

Ra		10^3	10^4	10^5	10^6
Grid used		(64×64)	(64×64)	(256×256)	(512×512)
U_{\max}	[14]	3.469	16.178	34.730	64.630
	Present	3.6529	16.163	35.521	64.186
Error (%)		5.301	0.09	0.599	0.685
Y	[14]	0.813	0.823	0.855	0.850
	Present	0.8125	0.828	0.8554	0.8496
Error (%)		0.06	0.622	0.05	0.045
V_{\max}	[14]	3.697	19.617	68.590	219.36
	Present	3.682	19.569	68.655	219.866
Error (%)		0.405	0.24	0.095	0.23
X	[14]	0.178	0.119	0.066	0.0379
	Present	0.17183	0.125	0.0664	0.0371
Error (%)		3.44	5.04	0.615	2.08
\overline{Nu}	[14]	1.118	2.243	4.519	8.800
	Present	1.121	2.286	4.5463	8.652
Error (%)		0.278	1.95	0.604	1.68
$Nu_{1/2}$	[14]	1.118	2.243	4.519	8.799
	Present	1.118	2.256	4.519	8.5074
Error (%)		0.053	0.579	0	3.31
Nu_0	[14]	1.117	2.238	4.509	8.817
	Present	1.1272	2.247	4.5226	8.805
Error (%)		0.193	0.408	0.3	0.135

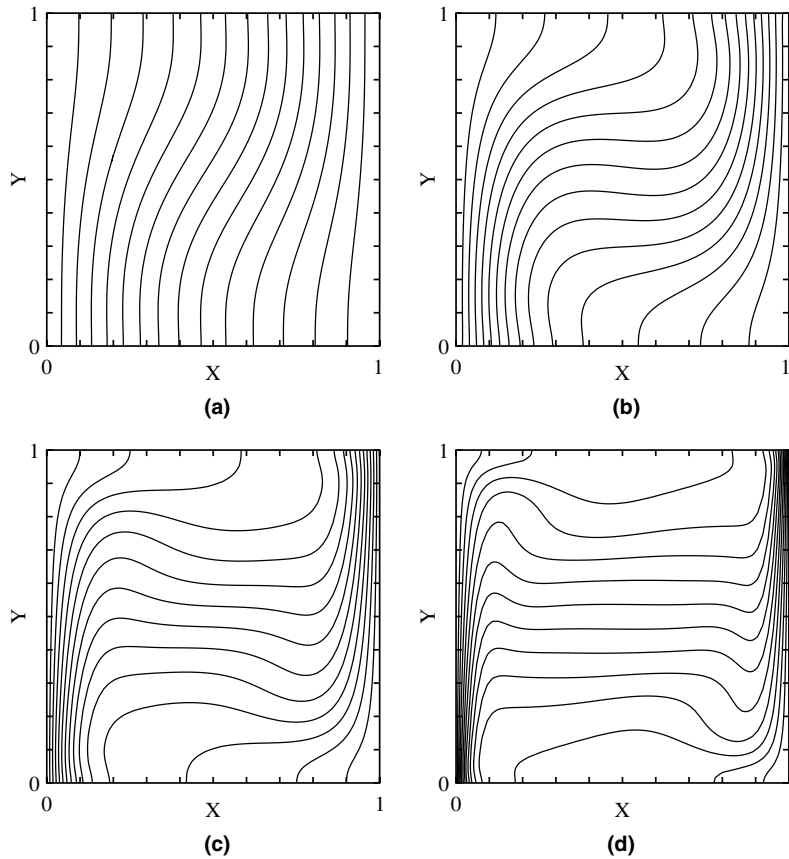


Fig. 3. Isotherms for (a) $Ra = 10^3$, (b) $Ra = 10^4$, (c) $Ra = 10^5$ and (d) $Ra = 10^6$.

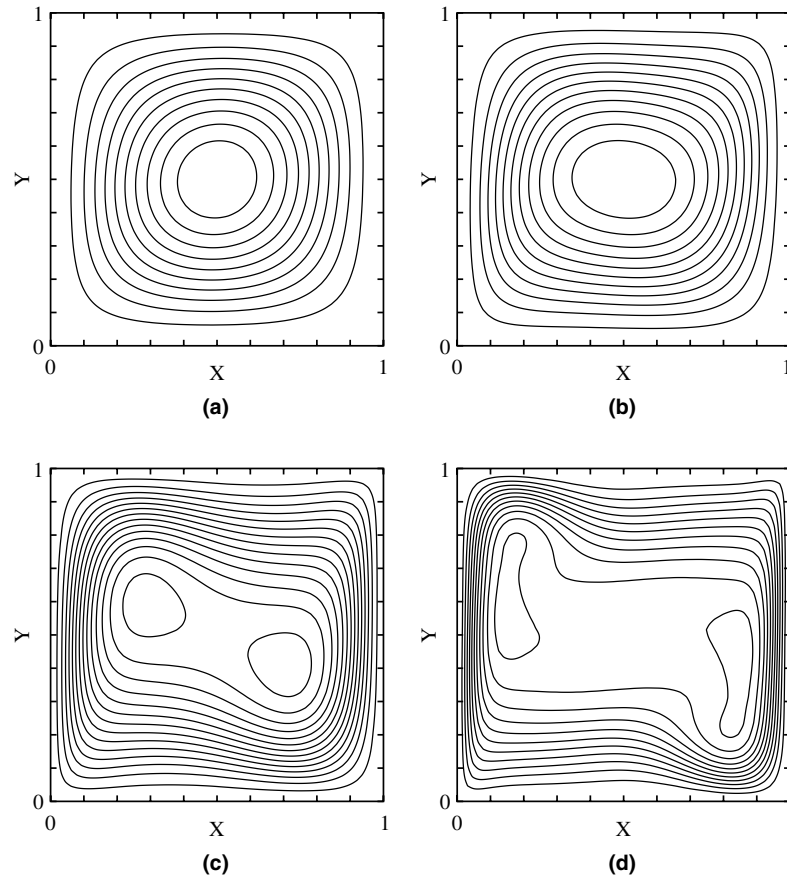


Fig. 4. Streamlines for (a) $Ra = 10^3$, (b) $Ra = 10^4$, (c) $Ra = 10^5$ and (d) $Ra = 10^6$.

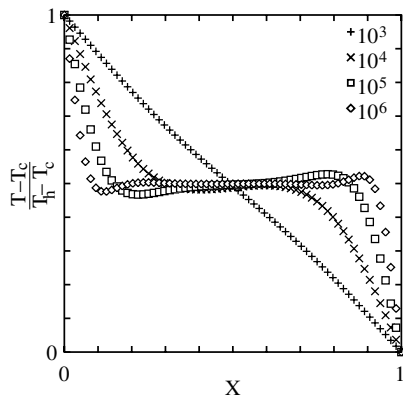


Fig. 5. Temperature profiles ($y/H = 0.5$) for $Ra = 10^3$ to $Ra = 10^6$.

Figs. 6 and 7 show the isotherms and stream lines for high Rayleigh number flows. It can be observed that, qualitatively they conform very well with the work of earlier groups using conventional CFD techniques employing turbulence models. The location of the separation and reattachment points as well as other major features of the flow field have been captured quite accurately by the ISLBM calculations.

Fig. 8(a) shows the variation of non-dimensional temperature, along the horizontal centerline of the cavity for

the transitional and turbulent flow simulations. A close-up view of the boundary layer near the left wall has been provided in Fig. 8(b). From this view, it can be observed that the steep gradients in the boundary layers are very well resolved.

4.4. Wall boundary layer profiles

With reference to the left wall of the cavity, the conventional scalings for the mean velocity profile in a turbulent boundary layer are given as $x^+ = xv^*/\nu$ and $v^+ = v/v^*$. Here v^* is the friction velocity defined as $v^* = (\nu \times \partial v / \partial x)^{1/2}$. Upon using the reference quantities given earlier, it can be easily shown that $x^+ = x(1/Pr \times \partial v / \partial x)^{1/2}$ and $v^+ = v / (Pr \times \partial v / \partial x)^{1/2}$. Here, all the quantities in the right hand side are dimensionless quantities. In this paper, x^+ has sometimes been referred to as y^+ with the usual connotation. Since the mean velocity profile is quite steep near the wall, the slope has to be estimated quite accurately. Here, the slope has been evaluated by fitting a linear regression line through the first 10 points.

Fig. 9 shows the variation of v^+ plotted against x^+ at $y/H = 0.1, 0.5$ and 0.8 on the hot wall. The local Grashof number is a function of y/H . It can be observed that the maximum value of v^+ at $y/H = 0.8$ is less than v^+ at $y/H = 0.5$, even though the corresponding Grashof number

Table 4

Comparison of the numerical results of the present study with the benchmark solution of Le Quéré [17] and Markatos and Pericleous [16]

Ra		10^7	10^8	10^9	10^{10}
Grid used		(256 × 256)	(256 × 256)	(512 × 512)	(512 × 512)
N_{char}		2048	3378	5440	12,000
U_{max}	[16]	–	514.3	–	2.323×10^3
	[17]	148.58	321.876	–	–
	Present	164.236	389.877	503.24	2.323×10^3
Y	[16]	–	0.941	–	0.9625
	[17]	0.879	0.928	–	–
	Present	0.851	0.937	0.966	0.940233
V_{max}	[16]	–	1812	–	1.689×10^4
	[17]	699.236	2222.39	–	–
	Present	701.922	2241.374	6820.07	2.1463×10^4
X	[16]	–	0.0135	–	0.0055
	[17]	0.021	0.012	–	–
	Present	0.020	0.0112	0.0064	0.49072
Nu_0	[16]	–	32.045	–	156.85
	[17]	16.523	30.225	–	–
	Present	16.79	30.506	57.350	103.663

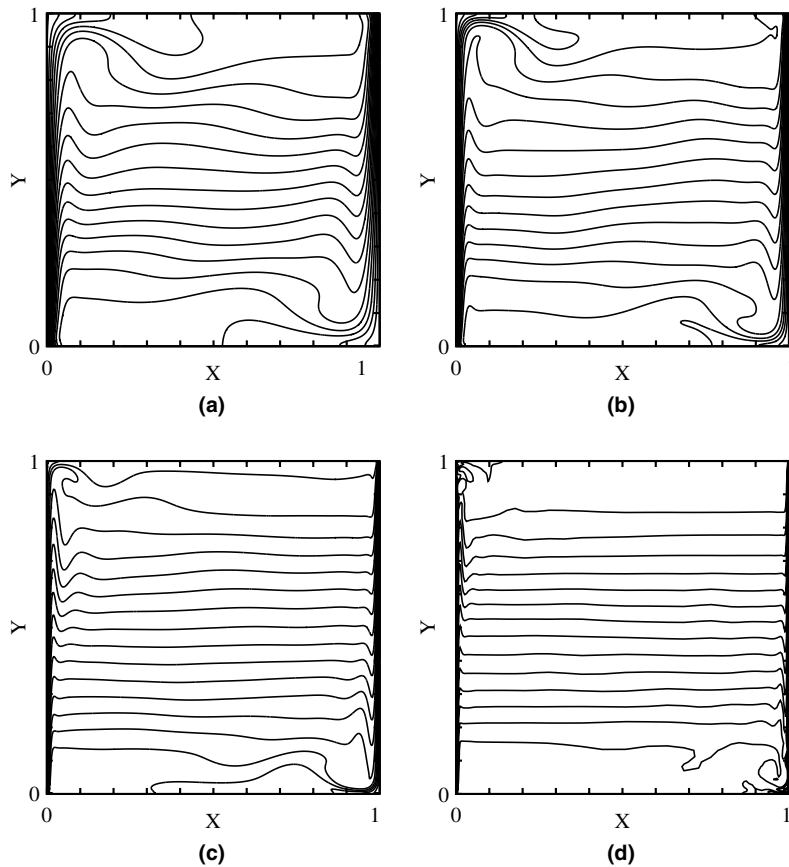


Fig. 6. Isotherms for (a) $Ra = 10^7$, (b) $Ra = 10^8$, (c) $Ra = 10^9$ and (d) $Ra = 10^{10}$.

at $y/H = 0.8$ is higher. This can be attributed to the presence of the top wall which causes the flow to slow down resulting in a lower value of v^+ . The variation of v^+ along the cold wall for the same Grashof numbers as plotted for

the hot wall are shown in Fig. 9. The corresponding values of y/H are 0.2, 0.5 and 0.9 (it should be kept in mind that the boundary layer develops from the top to the bottom now). It is clearly seen that the boundary layer profiles

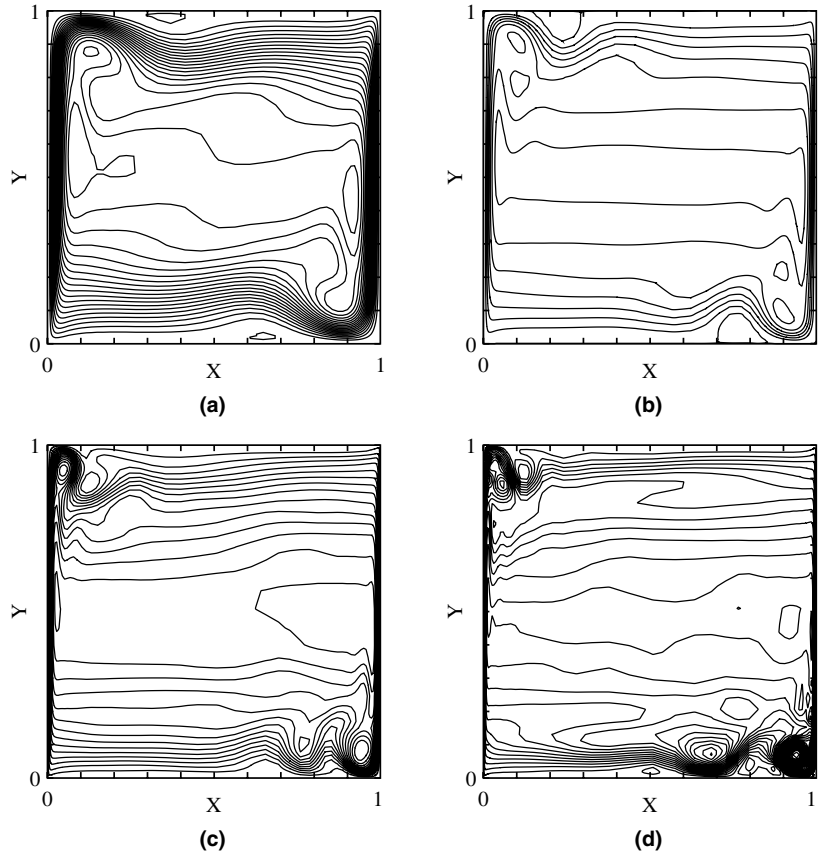


Fig. 7. Streamlines for (a) $Ra = 10^7$, (b) $Ra = 10^8$, (c) $Ra = 10^9$ and (d) $Ra = 10^{10}$.

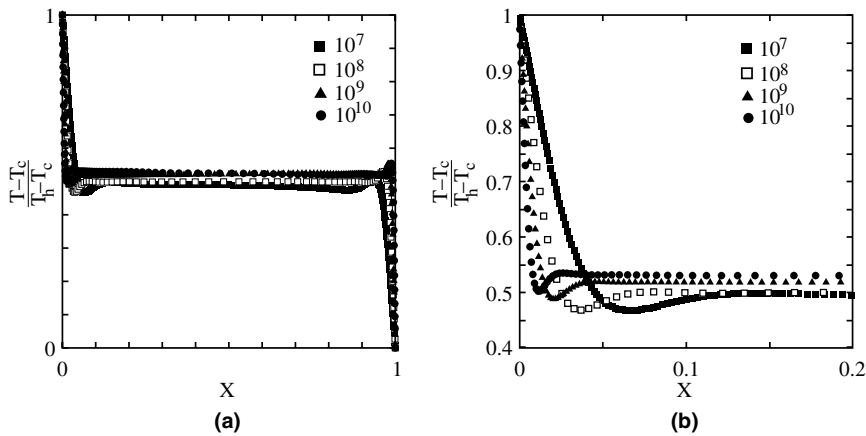


Fig. 8. Temperature profiles ($y/H = 0.5$) for $Ra = 10^7$ to $Ra = 10^{10}$: (a) for the entire cavity and (b) close-up view near the left wall.

on both the walls are identical. Again in this case, the presence of bottom wall results in a lower value for v^+ for $y/H = 0.2$ when compared with $y/H = 0.5$. Fig. 10 shows the variation of v^+ with x^+ at different values of y/H on the hot and cold walls for $Ra = 10^{10}$. The trends are very similar to those seen before for $Ra = 10^9$. Two striking features that are seen in Figs. 9 and 10 are

- wall x^+ values less than 0.3 and
- the collapsing of the profiles for $x^+ < 10$.

A comparison of the predicted profile of v^+ ($y/H = 0.5$) with the experimental results of Tsuji and Nagano [23] for natural convection over a vertical flat plate is given in Fig. 11. The experimental data also show the universal structure of the mean velocity profile for values of x^+ less than 10. The agreement between the current numerical predictions and the experimental data for $x^+ < 10$ is extremely good. This clearly demonstrates the ability of the LBM to predict such behavior ab initio, without resorting to turbulence models. The accurate prediction of the mean velocity

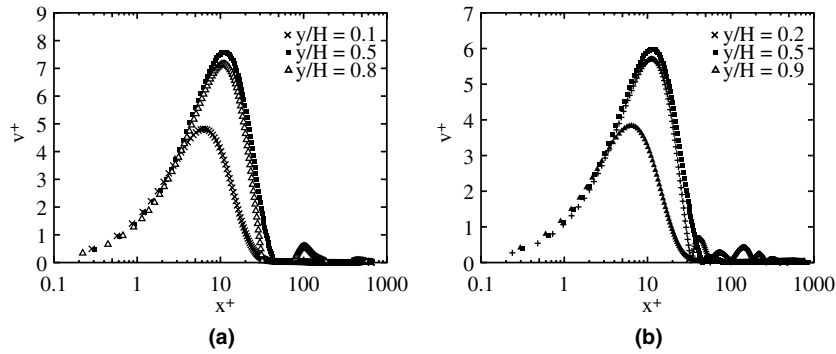


Fig. 9. Variation of v^+ for $Ra = 10^9$ along the wall: (a) hot wall and (b) cold wall.

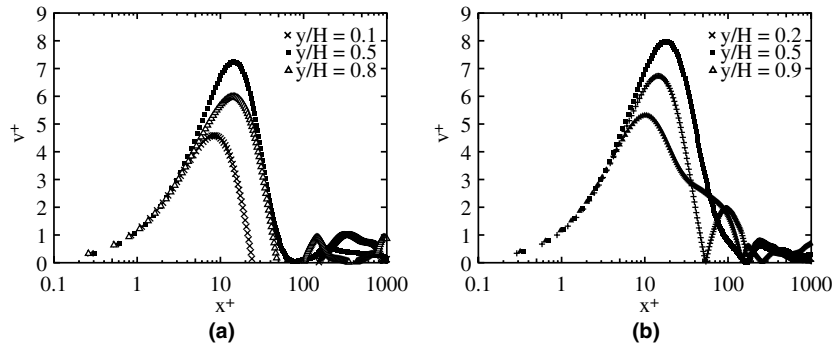


Fig. 10. Variation of v^+ along the hot wall for $Ra = 10^{10}$.

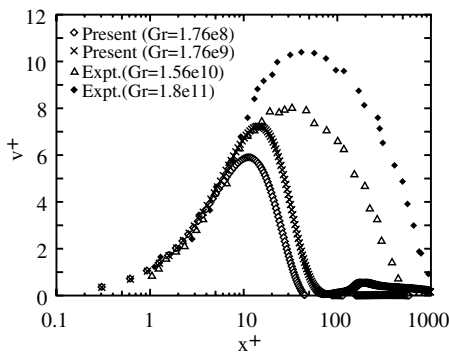


Fig. 11. Comparison of v^+ along the hot wall for $Ra = 10^9$ and 10^{10} with experimental results of Tsuji and Nagano [23].

profile in the turbulent layer is possible due to two reasons: one, the fine mesh near the wall, and two, accurate implementation of the no-slip and isothermal boundary conditions using the proposed extension of the counter-slip approach. An interesting aspect of the mean velocity profile in the present case is that the universal structure is seen for values of $x^+ < 10$ only, as opposed to $x^+ \approx 300$ in shear driven flows. This has important implications on the required refinement near the walls (i.e., wall y^+) for simulations of natural convection using standard wall functions. It is also important to note that such a comparison with experimental data has hitherto not been reported.

5. Summary and conclusions

Simulations of flow and temperature fields that arise due to natural convection in square and shallow cavities have been carried out using the lattice Boltzmann method. The salient features of the simulations are:

- the use of a non-uniform grid in conjunction with LBM,
- the proposed extension of the counter-slip approach for accurate implementation of the no-slip and isothermal boundary conditions,
- the absence of a turbulence model for the turbulent flow calculations,
- wall y^+ values less than 0.3.

The numerical solutions are able to capture the velocity and temperature gradients accurately owing to the fine grids used. Laminar results compare very well with the bench-mark results of de Vahl Davis [14] and the turbulent results compare favorably with the work of Markatos and Pericleous [16] and bench-mark results of Le Quéré [17].

The accuracy of the present simulations are extremely good till $Ra = 10^8$. Beyond this, there is a small discrepancy in the calculated values of Nusselt number, though the maximum values for velocities are fairly accurate. This is most likely due to the unsteadiness of the flow at these Rayleigh numbers. Another contributing factor could be

the polynomial equilibrium distribution for temperature which is only $O(u)$ accurate unlike the isothermal model which is accurate up to $O(u^2)$.

Use of the ISLBM, alleviated this difficulty to a large extent. Even though only second order Lagrangian interpolation has been used in the present study, the results are accurate enough for engineering simulations. But at higher Rayleigh numbers, especially for $Ra = 10^{10}$, the convergence was extremely slow. Since no turbulence modeling is employed in the present simulations, the times taken for the high Rayleigh number simulations are on the higher side. This is partially mitigated by the inherent parallelism of the ISLBM computations [24], which allows machine speeds for scalar computations and super-linear speedup for parallel computations to be realized. For lower Rayleigh number flows, especially up to 10^8 , the method is extremely competitive for these kind of flows both in terms of accuracy and speed.

The most significant finding of this work is the capability of the LBM to predict the mean velocity turbulent boundary layer profile accurately. The present LBM calculations are akin to DNS on account of the fact that no turbulence model has been used. It is well known that buoyancy induced turbulence is even more difficult to simulate numerically than shear induced turbulence. In this light, the above finding represents a significant breakthrough in numerical simulations of such flows. It is very interesting to note that LBM calculations should be able to predict not only mean quantities but fluctuating quantities, such as TKE, turbulent shear stresses etc., as well. Of course, this would require enormous amount of data storage and processing. For example, a 512×512 grid will require 4 MB of data to be stored per time step (two velocity components each requiring eight bytes in double precision and quarter-of-a-million points). The calculations are usually run for millions of time steps. With SANs of storage capacity of several Terabytes and high band-width connections available these days, the above mentioned task should be possible in the near future.

Though many of the advantages of LBM are due to the simplicity of the BGK collision model, it is also a serious limitation, since Prandtl numbers that can be simulated are restricted to be around 1/2. More sophisticated collision operators like the multiple-relaxation time collision operator proposed by d'Humières [25] can be employed where individual relaxation parameters could be tuned to achieve variable Prandtl numbers, or the two-step relaxation process where the problem of fixed Prandtl number can be alleviated to a certain extent. Another limitation of LBM is the use of polynomial expressions for the equilibrium distribution. It has recently been shown that H -theorem is not satisfied if a polynomial equilibria is used [26]. Better models obeying the H -theorem [27] are being developed where a non-polynomial equilibria is employed. Rigorous numerical tests need to be carried out to prove the usefulness of these models.

Acknowledgements

The authors would like to thank the Computer Centre, IIT Madras for granting time on their SGI Origin 3000 and IBMp690. HND would like to thank C. Shyam Sunder, IIT Madras and Ms. Annunziata D'Orazio, Università di Roma "La Sapienza", for discussions and many helpful suggestions during the course of the work. The authors would also like to thank the reviewers for their constructive comments and suggestions.

References

- [1] S. Chen, G.D. Doolen, Lattice Boltzmann method for fluid flows, *Ann. Rev. Fluid Mech.* 30 (1998) 329–364.
- [2] S. Succi, *Lattice Boltzmann Method for Fluid Dynamics and Beyond*, Oxford University Press, 2001.
- [3] Y. Peng, C. Shu, Y.T. Chew, Simplified thermal lattice Boltzmann model for incompressible thermal flows, *Phys. Rev. E* 68 (2003) 026701.
- [4] A. D'Orazio, M. Corcione, G.P. Celata, Application to natural convection enclosed flows of a lattice Boltzmann BGK model coupled with a general purpose thermal boundary condition, *Int. J. Therm. Sci.* 43 (2004) 575–586.
- [5] Y. Zhou, R. Zhang, I. Staroselsky, H. Chen, Numerical simulation of laminar and turbulent buoyancy-driven flows using a lattice Boltzmann based algorithm, *Int. J. Heat Mass Transfer* 47 (2004) 4869–4879.
- [6] F.J. Alexander, S. Chen, J.D. Sterling, Lattice Boltzmann thermohydrodynamics, *Phys. Rev. E* 47 (1993) 2249–2252.
- [7] Y. Chen, H. Ohashi, M. Akiyama, Thermal lattice Bhatnagar–Gross–Krook model without nonlinear deviations in macrodynamic equations, *Phys. Rev. E* 50 (1994) 2776–2783.
- [8] J.G.M. Eggels, J.A. Somers, Numerical simulation of free convection flow using the lattice Boltzmann scheme, *Int. J. Heat Fluid Flow* 16 (1995) 357–364.
- [9] G. McNamara, A.L. Garcia, B.J. Alder, Stabilization of thermal lattice Boltzmann models, *J. Stat. Phys.* 91 (1995) 395–408.
- [10] F. Massaioli, R. Benzi, S. Succi, Exponential tails in two-dimensional Rayleigh–Bénard convection, *Europhys. Lett.* 21 (3) (1993) 305.
- [11] X. Shan, Simulation of Rayleigh–Bernard convection using a lattice Boltzmann method, *Phys. Rev. E* 55 (1997) 2780–2788.
- [12] X. He, L.S. Luo, Theory of the lattice Boltzmann method: from Boltzmann equation to the lattice Boltzmann equation, *Phys. Rev. E* 56 (6) (1997) 6811–6817.
- [13] X. He, S. Chen, G.D. Doolen, A novel thermal model for the lattice Boltzmann method in incompressible limit, *J. Comput. Phys.* 146 (1998) 282–300.
- [14] G. de Vahl Davis, Natural convection of air in a square cavity: a benchmark numerical solution, *Int. J. Numer. Meth. Fluids* 3 (1983) 249–264.
- [15] R.A.W.M. Henkes, C.J. Hoogendoorn, Scaling of the laminar natural-convection flow in a heated square cavity, *Int. J. Heat Mass Transfer* 36 (1992) 2913–2925.
- [16] N.C. Markatos, K.A. Pericleous, Laminar and turbulent natural convection in an enclosed cavity, *Int. J. Heat Mass Transfer* 27 (1984) 755–772.
- [17] P. Le Quééré, Accurate solutions to the square thermally driven cavity at high Rayleigh number, *Comput. Fluids* 20 (1991) 29–41.
- [18] F. Nannelli, S. Succi, The lattice Boltzmann equation on irregular lattices, *J. Stat. Phys.* 68 (3) (1991) 401–407.
- [19] X. He, L.S. Luo, M. Dembo, Some progress in lattice Boltzmann method. Part I. Nonuniform mesh grids, *J. Comput. Phys.* 129 (1996) 357–363.

- [20] T. Inamuro, M. Yoshino, F. Ogino, A non-slip boundary condition for lattice Boltzmann simulations, *Phys. Fluids* 7 (1995) 2928–2930.
- [21] X. He, Q. Zou, L.S. Luo, M. Dembo, Analytic solutions of simple flows and analysis of nonslip boundary condition for the lattice Boltzmann BGK model, *J. Stat. Phys.* 87 (1997) 115–136.
- [22] H.N. Dixit, Simulation of flow and temperature fields in enclosures using the lattice Boltzmann method. MS Thesis, 2005, Indian Institute of Technology Madras, India.
- [23] T. Tsuji, Y. Nagano, Characteristics of a turbulent natural convection boundary layer along a vertical flat plate, *Int. J. Heat Mass Transfer* 31 (8) (1988) 1723–1734.
- [24] C. Shyam Sunder, G. Baskar, V. Babu, D. Strenski, Parallel performance of the interpolation supplemented lattice Boltzmann method. *Lecture Notes in Computer Science*, 2913, Springer-Verlag, Berlin, 2000, pp. 428–437.
- [25] D. d’Humières, Generalized lattice Boltzmann equations, in: B.D. Shizgal, D.P. Weaver (Eds.), *Rarefied gas dynamics: theory and simulations*, *Prog. Aeronaut. Astronaut.* 159 (1992) 450–458.
- [26] W.A. Yong, L.S. Luo, Nonexistence of H theorems for the athermal lattice Boltzmann models with polynomial equilibria, *Phys. Rev. E* 67 (5) (2003) 051105.
- [27] I.V. Karlin, S. Succi, Equilibria for discrete kinetic equations, *Phys. Rev. E* 58 (4) (1998) R4053.